Variable Gain DNA Nanostructure Charge Amplifiers for Biosensing

Jacob M. Majikes[1], Seulki Cho[1], Thomas E. Cleveland IV[2,3], J. Alexander Liddle[1] and Arvind Balijepalli[1]

[1]Microsystems and Nanotechnology Division
National Institute of Standards and Technology, Gaithersburg MD 20899
[2]Biomolecular Measurement Division,
National Institute of Standards and Technology,
Gaithersburg, MD 20899
[3]Institute for Bioscience and Biotechnology Research,
University of Maryland, Rockville, MD 20850
e-mail: arvind.balijepalli@nist.gov

Keywords: DNA nanotechnology, self-assembly, electronic sensing, EIS, signal amplification

Abstract: Electronic measurements of engineered nanostructures comprised solely of DNA (DNA origami) enable new signal conditioning modalities for use in biosensing. DNA origami, designed to take on arbitrary shapes and allow programmable motion triggered by conjugated biomolecules, have sufficient mass and charge to generate a large electrochemical signal. Here, we demonstrate the ability to electrostatically control the DNA origami conformation, and thereby the resulting signal amplification, when the structure binds a nucleic acid analyte. Critically, unlike previous studies that employ DNA origami to amplify an electrical signal, we show that the conformation changes under an applied field are reversible. This applied field also simultaneously accelerates structural transitions above the rate determined by thermal motion. We tuned this property of the structures to achieve a response that was $\approx 2\times10^4$ times greater (i.e., a gain or amplification) than the value from DNA hybridization under similar conditions. Because this signal amplification is independent of DNA origami-analyte interactions, our approach is agnostic of the end application. Furthermore, since large signal changes are only triggered in response to desirable interactions, we minimize the deleterious effects of non-specific binding. The above benefits of self-assembled DNA origami make them ideally suited for multiplexed biosensing when paired with highly parallel electronic readout.

DNA origami[1] that can perform local signal conditioning such as amplification have the potential to drastically improve biochemical sensing by improving sensitivity to molecules of interest. These structures are assembled by hybridizing synthetic DNA with a viral scaffold that allows it to 'fold' into a predetermined shape. The predetermined shapes of DNA origami can be designed to specification in one of many Computer Aided Design (CAD) tools, with well-established techniques controlling for critical attributes such as local rigidity and dynamic motion.[2] Importantly, DNA origami can be interfaced with a broad range of commercially available DNA bioconjugation chemistries to allow attachment of nanoparticles and biomolecules at arbitrary locations with molecular precision.[3] Therefore, DNA origami can serve as a crucial component

in a platform for electrochemical sensing because of their modularity and flexibility, which allows them to be rapidly reengineered for new biomolecular binding targets.

To date, a wide array of biosensing proofs-of-concept have utilized these capabilities.[4] The vast majority of the signals generated by these structures are transduced optically, typically through Förster Resonance Energy Transfer (FRET), although several other schemes exist, such as gel mobility,[5] circular dichroism,[6] movement of light-visible nanoparticles,[5] spectroscopy[7,8] and triggered polymerization.[9] There have also been studies that measure the motion of DNA origami *via* changes in the electrochemical potential, for example the actuation of structures using pH,[10,11] AC electric field driven motion of DNA nanorods measured optically,[12] electrochemical measurements of DNA origami,[11,13–16] or capacitance measurements to track their assembly.[17] In addition, it is not uncommon to use DNA functionalized nanoscale materials to amplify signal response, ranging from the covalent attachment of redox mediators,[18,19] to sandwich assay strategies with enzymes whose activity is detected electrochemically.[20]

While novel, these demonstrations often fall short of the full potential of DNA nanotechnology in biochemical sensing. There are several established routes to achieving chemical specificity for biosensing.[21–23] Therefore, the benefits of incorporating DNA origami must outweigh the increase in system complexity,[24] and the high per-mole cost of DNA origami. Previous electrochemical studies[11,13–16] have established the signal amplification with DNA origami. However, improved sensitivity is not the only grand challenge facing biosensing.[25] As we show here, the ability to amplify the measured signal reversibly and to control this amplification *via* an applied electric field allow far more control and precision than previously demonstrated. The ability to engineer these precise interactions within a modular platform will open new avenues to streamlined multiplexed detection.

Here we explore the design space by examining the signal response of two different DNA origami whose mechanical properties have been previously characterized.[26,27] We test the function of these DNA origami under an applied electric field and measure its effect in altering their conformation upon binding an analyte. This conformational change displaces a large amount of charge and results in robust amplification of the transduced signal. Critically, we show that the applied electric field can control the overall signal amplification by shifting the equilibrium angle of the hinge and therefore the capacitance of the structure. Finally, the applied electric field can speed up the transition from the starting to final conformations and provides an additional measure of control that determines signal amplification.

Results and Discussion

Structural Characterization. The DNA origami used in this study take the form of a hinge found in the literature.[27] We chose this structure, in part, because its original application in force

spectroscopy necessitated a characterization of the hinge angle distribution as well as its mechanical properties.[26,28] This characterization made it easier to adapt it for electrochemical sensing applications while providing some assurance of its baseline performance.

The DNA origami is comprised of two arms connected by eight short single stranded DNA (ssDNA) tethers as seen in Fig. 1A. Each arm consists of 20 double stranded DNA (dsDNA) helices arranged in three layers in an 8–4–8 configuration. Each arm has a lock motif placed ≈12 nm from the hinge. This feature allows an analyte, for example a ssDNA strand with a sequence complementary to the lock strand, to trigger actuation of the structure. The bottom arm is connected to the electrode surface at nine locations using dsDNA tethers or stilts that are 25 nucleotides (≈8.3 nm) long. Representative images from cryogenic electron microscopy (cryo-EM) that were used to validate the structures are shown in Fig. 1B with full fields of view in the *Supplementary Information* (SI) section S7. Individual cryo-EM images were combined (SI section S8) to produce a partial 3D-reconstruction (Fig. 1C) that validates the cross-section of the DNA origami. Because the hinge halves are flexible and are comprised of identical repeating regions the cryo-EM reconstruction shows only one such repeating region that is ≈24 nm long. Because there is a mismatch in the mapping between the desired connections and the relaxed helicity of B-form DNA, enforcing a structure that lies on a square grid can result in internal strain and mild torsion as seen in Fig. 1C. This strain was partially alleviated through modulation of the number of bases between helices. However, our results indicate that some residual strain remained in the structures that resulted in mild torsion.

The mild torsion experienced by the DNA origami structure was not found to be detrimental to the force spectroscopy applications for which it was originally designed[27] or, as evidenced by the measured gain discussed below, for its use as a signal amplifier. Given the complexities of designing an articulating 3D DNA origami, our choice to modify an existing structure allowed us to focus on making a novel measurement system that can form a critical component in biosensing. The minimal effort required to adapt this structure for biosensing applications highlights the modularity and customization possible when using DNA origami.

The lock motifs (SI section S1) were designed to create two variants, one that remains open (*normally open*) and another that remains closed (*normally closed*) in the absence of a complementary ssDNA sequence. Steric design constraints require the lock motif for the *normally closed* case to be twice as long as the *normally open* case. Therefore, the *normally closed* structure has a starting angle (in the absence of analyte) of ≈ π/6 rad (30°) and a final angle of ≈ 7/18 π rad (70°) when released upon binding an analyte.[27] The *normally open* structure has a starting angle approaching ≈ 7/18 π rad (70°) and closes more tightly upon exposure to an analyte, to ≈ π/12 rad (15°) due to its shorter lock motif.

The modularity of DNA origami affords tremendous flexibility in the design of the lock motif and its placement on the structure. In its current form, the lock is well-suited for the types of small nucleic acid analytes used in this study. Several optimizations are available to adapt the lock that are partly dependent on the end application. The position of the lock relative to the hinge can be used to change the closing angle of the structure and thereby optimize the gain of the signal amplification. Alternatively, placing the lock on the side of the top and bottom leaflets can be used to improve solution accessibility and improve response times. Additionally, multiple locks can be engineered to signal when certain logic conditions are satisfied, for example if multiple analyte types are present and bind the structure simultaneously. Finally, the structures can target other analyte types such as proteins or small molecules by implementing one of several DNA bioconjugation strategies . One straightforward approach is to split an aptamer into two halves, each attached to one leaflet of the DNA origami such that the presence of a target analyte induces a conformational change in the structure.[29] More generally, the top and bottom of the lock halves can be covalently attached to ligands that simultaneously bind a target to like those used in sandwich assays while triggering a conformation.

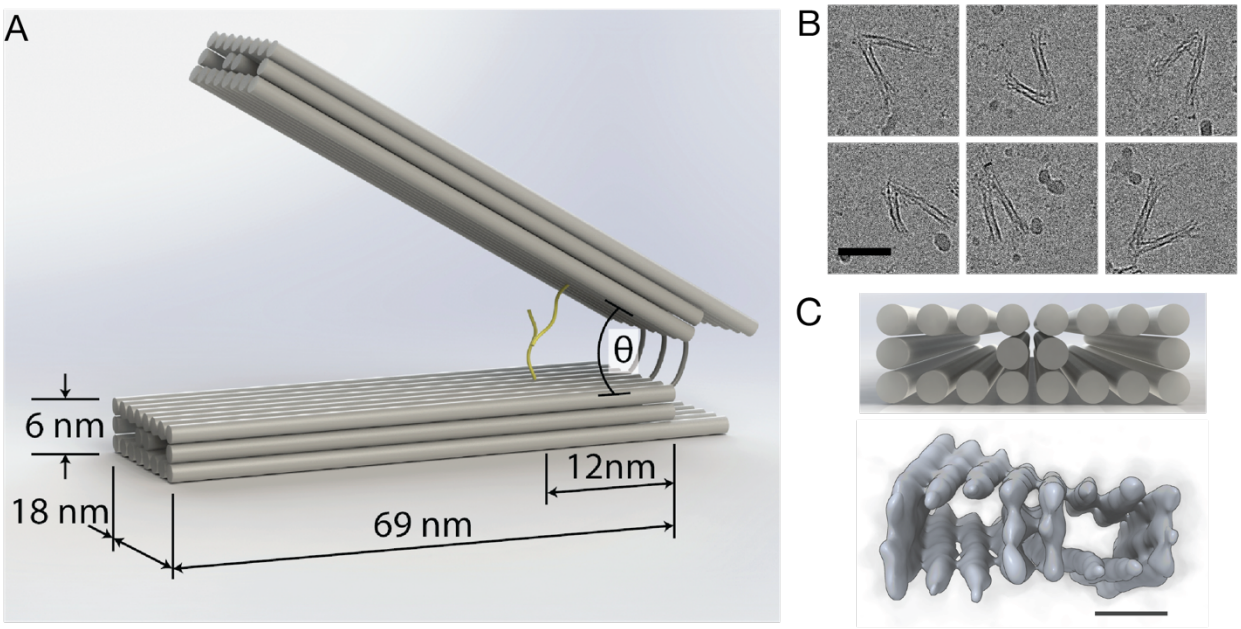

Fig. 1: (A) Schematic representation of the DNA origami that shows the two arms of the hinge and the lock strands (*yellow*) that interact with a complementary DNA analyte. (B) Representative cryogenic electron microscopy (cryo-EM) images of the DNA origami. The scale bar is 50 nm. (C) Cross-sectional schematic and three-dimensional reconstruction of a hinge half from cryo-EM images. The scale bar is 6 nm.

Electrochemical Measurements of Function. We tested the function of the *normally closed* (Fig. 2A) and *normally open* (Fig. 2B) structures by using electrochemical impedance spectroscopy (EIS). In each case, we functionalized a gold electrode with the DNA origami and validated attachment as described in the *Methods* section. We measured the DNA origami in the absence of analyte (*blue*) and compared them to measurements in the presence of 1 nmol/L

(1 nM) analyte that had a complementary sequence to the lock strand (*orange*). In all cases the applied DC bias was 0 V and the analyte was incubated for 60 minutes to allow sufficient time to bind the DNA origami. By fitting a simplified Randles circuit model[30] to the EIS data, we extracted the circuit parameters for each DNA nanostructure type (parameter table in SI section S2). For both structures we observed an increase in capacitance from a baseline value with no analyte present [*normally closed*, (119±1) nF; *normally open*, (99±1) nF] to an ≈ 20 % higher value when exposed to the analyte for 60 minutes [*normally closed*, (143±2) nF; *normally open*, (117±3) nF]. In contrast, the capacitance for ssDNA probe molecules[14] increased by a smaller amount from a baseline value of (38.7±0.3) nF to (41.4±0.6) nF when exposed to the analyte for 60 minutes (SI section S2). In all cases, the reported expanded uncertainties in the EIS fit parameters from three independent measurements have a coverage factor k=2 (95 % confidence interval). To understand the increase in capacitance for both DNA origami we devised a simple model and complementary measurements under an electric field that are discussed next.

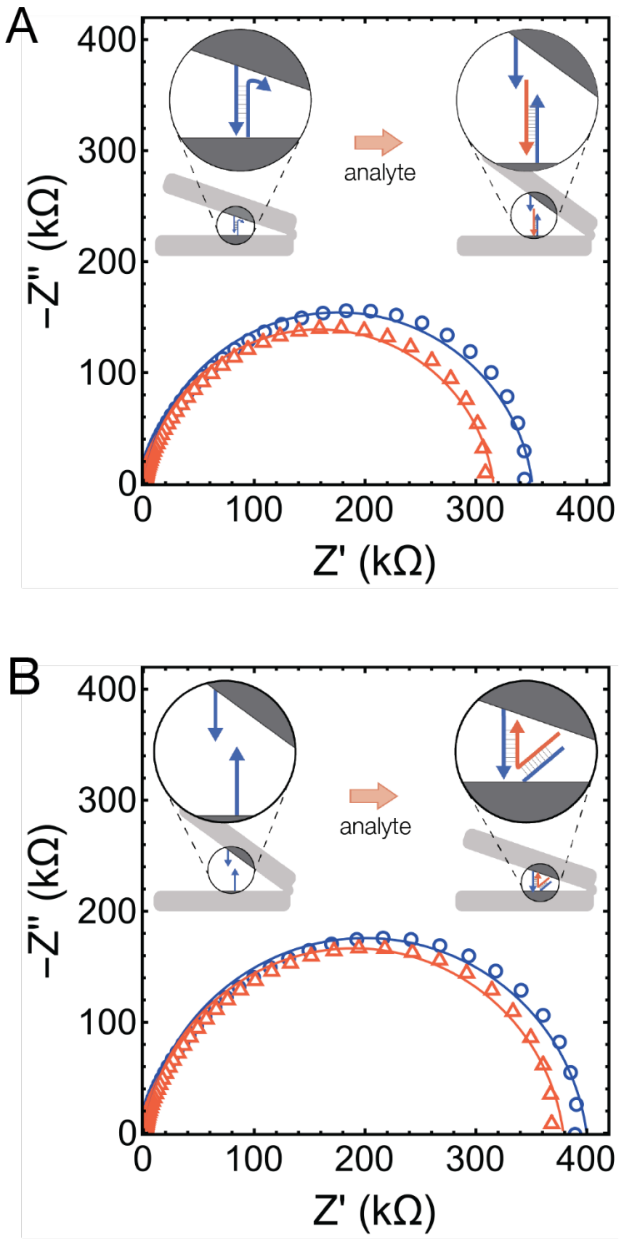

Fig. 2: Electrochemical impedance spectroscopy (EIS) of (A) *normally closed* and (B) *normally open* DNA origami in the absence (*blue*) and presence of 1 nmol/L (nM) analyte (*orange*) that has a sequence complementary to the lock strand. Solid lines in each case represent fits of a simplified Randles circuit model. (*insets*) Representation of the starting and final state for each DNA nanostructure variant upon adding a complementary DNA sequence (*orange*) that binds the lock strands (*blue*) A representative measurement is shown here. Full data sets from three independent measurements used to estimate fit parameters are shown in the Supplementary Information (section S2).

Capacitance Circuit Model. Fig. 3A shows a schematic and corresponding circuit model of the DNA origami that allows us to describe the dependence of their measured capacitance ($C_{structure}$) on the angle of the hinge (θ), which can be altered by changing the applied DC voltage (V_{DC}). Total capacitance (C_t) as a function of θ (see SI section S4 for the derivation) was,

$$C_t(\theta) = \varepsilon\varepsilon_0 d\left(\frac{l(1-cos(\theta))}{h} + \frac{1}{\frac{h\,(\sec(\theta)+\tan(\theta))}{l} + \frac{\sin(\theta)}{\log(w_h + l\cos(\theta)\sin(\theta)) - \log(w_h)}}\right) \qquad (1),$$

where l is the length of the DNA nanostructure, d is its depth, h is the height of each arm, w_h is the height of the electrolyte layer when the structure is fully closed, ε is the dielectric constant and ε_0 is the vacuum permittivity. Using the dimensional parameters from Fig. 1 and an estimate of the density of the DNA origami on the electrode surface (SI section S9), we plot C_t as a function of θ in Fig. 3B. The *blue* line in Fig. 3B shows the expected neutral angle for the *normally closed* structure at V_{DC}=0 V. From Fig. 3 we observe that the expression for C_t qualitatively captures the capacitance behavior as the DNA nanostructure transitions from a closed to an open conformation by the applied electric field. As the structure is closed C_t increases due to the thinning of the electrolyte layer encompassed by the two arms. Conversely, the structure opening results in a broad minimum followed by a slight increase in C_t as θ approaches $\pi/2$ rad (90°). This increase in C_t is dominated by the capacitance of the bottom arm as it is exposed to the electrolyte solution when the top arm retracts. This effect of the contribution of the bottom arm to C_t is observed from the dashed line in Fig. 3B, which was estimated by suppressing the second term in Eq. 1.

The analysis was validated by measuring $C_{structure}$ of the *normally closed* case as a function of V_{DC} in Fig. 3C. The measurements were corrected for the passivation of the electrode surface and the electrical double layer as described in the SI section S3. The mapping of θ onto V_{DC} was assumed to be linear and piecewise as described in Eq. 2, where θ_n is the neutral design angle of the DNA nanostructure, V_{max} is the maximum applied voltage, θ_{mn} is the minimum closing angle under positive voltages and θ_{mx} is the maximum opening angle under negative applied voltages.

$$\theta(V_{DC}) = \begin{cases} \theta_n + \frac{|V_{DC} - V_{Ag/AgCl}|}{|V_{max}|}\theta_{mx}, & V_{DC} < 0 \\ \theta_n - \frac{|V_{DC} - V_{Ag/AgCl}|}{|V_{max}|}\theta_{mn}, & V_{DC} \geq 0 \end{cases} \qquad (2)$$

In Fig. 3C, by fitting the model described by Eq. 1 and Eq. 2 (solid *blue* line) to the data for the *normally closed* structure we estimated θ_n=(0.54±0.03) rad [(31±2)°], θ_{mn}=(0.40±0.05) rad [(23±3)°], θ_{mx}=(0.26±0.03) rad [(15±2)°] when V_{max}=0.4 V. These parameters translate into range of motion from (0.29±0.04) rad or (16±2)° when the DNA nanostructure is fully closed at V_{DC}–$V_{Ag/AgCl}$=+0.4 V to (0.96±0.06) rad or (55±3)° when it is open at V_{DC}–$V_{Ag/AgCl}$=–0.4 V. The upper limit of the hinge angle at negative voltages predicted by the model is consistent with the expected reduction in efficiency of the electrical field in actuating the structures as discussed in more detail later (see Fig. 4). While model fit captures the data in Fig. 3C well, it does not adequately capture the broad peak centered at V_{DC}–$V_{Ag/AgCl}$≈ 0.15 V, which is discussed next.

Finally, results for the *normally open* case exhibit a similar trend to the data in Fig. 3C and are shown in the SI section S3.

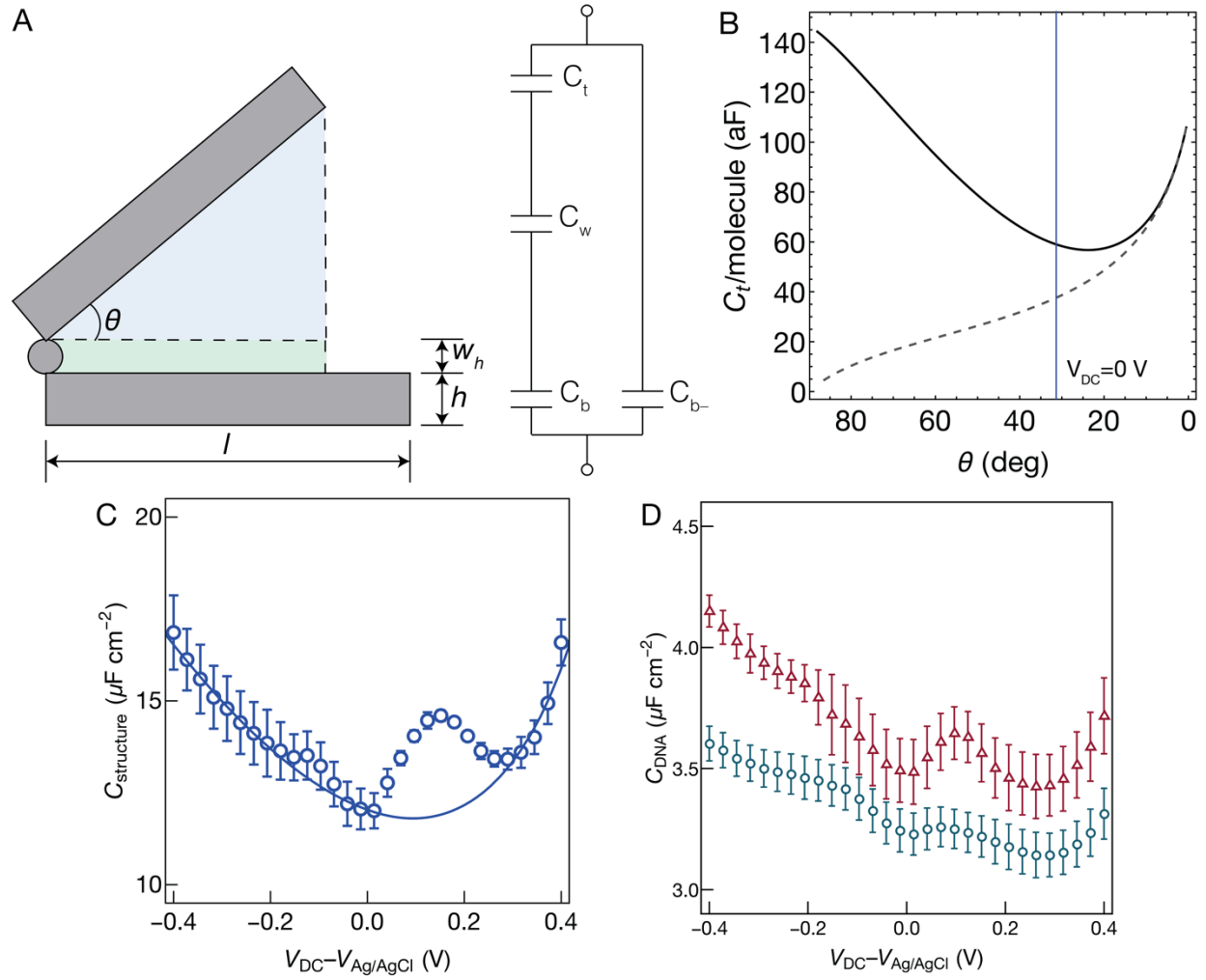

Fig. 3: Measurements and modeling of the capacitance of DNA origami as a function of applied DC bias (V_{DC}–$V_{Ag/AgCl}$) relative to an AgCl reference electrode. (A) Schematic and equivalent circuit model of a DNA origami. (B) Modeled capacitance per origami molecule computed using Eq. 1 and Eq. 2. C_t, as a function of hinge angle, θ inferred by solving the equivalent circuit in panel A. (C) Capacitance measurements vs. V_{DC}–$V_{Ag/AgCl}$ of *normally closed* (*blue*) DNA origami ($C_{structure}$) conjugated to a gold surface in the absence of analyte. The capacitance was measured with an applied AC field with a frequency of 100 Hz and amplitude V_{pk}=20 mV summed with V_{DC}–$V_{Ag/AgCl}$. The solid line is a fit of the model to the data. (D) Capacitance measurements vs. V_{DC}–$V_{Ag/AgCl}$ of DNA probe strands (C_{DNA}), with identical sequence to the DNA nanostructure lock, in the absence (*green*) and presence of 1 nM (nmol/L) analyte (*red*). For all plots in the figure, three independent measurements were used to estimate the expanded uncertainties are reported with coverage factor k=2 (95 % confidence interval).

Impact of E-Field on dsDNA Spacers. An interesting feature of the plot in Fig. 3C is the presence of the peak centered at V_{DC}–$V_{Ag/AgCl} \approx 0.15$ V and is not captured by the model shown by Eq. 1. Such behavior has been previously observed when using electric fields to force dsDNA to lie flat on a surface and was found to occur at comparable values of applied voltage for both

DNA origami tested in this study.[31,32] We believe the peak in Fig. 3C is associated with pulling down the nine dsDNA tethers that anchor the structures to the gold surface (Fig. S5.1). To further validate this hypothesis, we hybridized the ssDNA with an analyte with complementary sequence and measured C_{DNA} as a function of V_{DC}–$V_{Ag/AgCl}$ as seen in Fig. 3D. While we observed no peak for the ssDNA case (*green*), we clearly see the emergence of a new peak at ≈0.15 V (*red*) upon hybridizing the ssDNA with a complementary strand. Furthermore, the location of this peak at ≈0.15 V is consistent with the capacitance data in Fig. 3C for the DNA nanostructure strongly indicating that it is related to the electrical field forcing the nine dsDNA tethers in the structure to lie flat on the electrode surface.

Capacitance Changes upon Binding Analyte. The change in the capacitance with applied electric field discussed previously can also be initiated by binding a nucleic acid that has a complementary sequence with the lock strand for the *normally open* or *normally closed* structures. While a large change in the measured capacitance upon analyte binding should occur at equilibrium, reaching this state can take a significant amount of time requiring longer incubation (e.g., 60 minutes used in Fig. 2).[33] This would preclude the structures from use in practical applications such as clinical diagnostics. Here we show that the applied electrical field can be used to accelerate the kinetics of the hinge transition. For both the *normally closed* and *normally open* cases we measured the change in capacitance as a function of V_{DC}–$V_{Ag/AgCl}$ in Fig. 4. In each case the measurements were limited to an incubation time of 15 minutes.

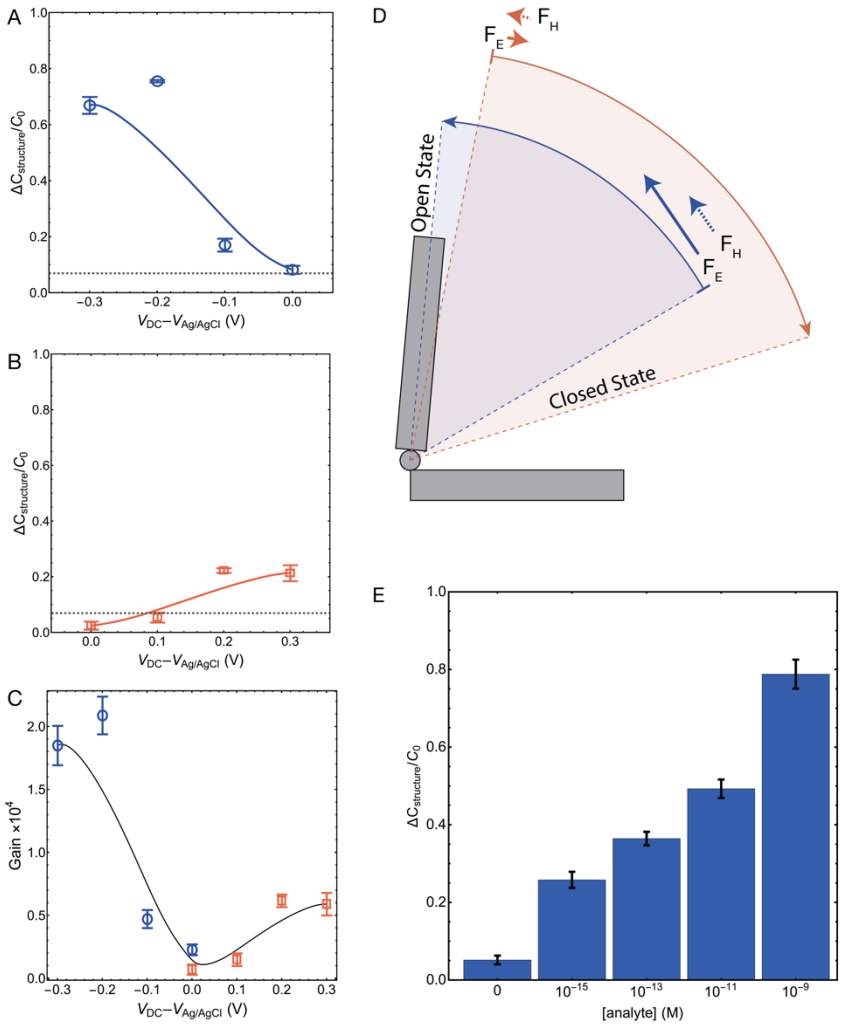

Fig. 4: Relative change in capacitance ($\Delta C_{structure}/C_0$), where C_0 is the initial capacitance and gain of DNA origami relative to the change in capacitance of DNA hybridization (ΔC_{ssDNA}). (A) and (B) $\Delta C_{structure}/C_0$ of the *normally closed* and *normally open* DNA origami in the presence of 1 nM (nmol/L) analyte as a function of the DC bias ($V_{DC}-V_{Ag/AgCl}$) relative to the absence of analyte. The dashed lines in each panel show ΔC_{ssDNA} in the presence of 1 nM (nmol/L) of DNA analyte. (C) Gain (G) of the *normally closed* (*blue*) and *normally open* (*orange*) DNA origami over the DNA hybridization case. (D) Schematic of the forces from the hinge spring constant, F_H, and the portion of electric force normal to the hinge, F_E, at the relevant angles for the two structures as described in the main text. (E) $\Delta C_{structure}/C_0$ as a function of the analyte concentration in solution. The zero-concentration case represents a control with a non-complementary sequence. For all plots in the figure, three independent measurements were used to estimate expanded uncertainties are reported with coverage factor k=2 (95 % confidence interval).

Fig. 4A shows the relative change in the DNA origami capacitance ($\Delta C_{structure}/C_0$) for the *normally closed* structures after incubation with 1 nmol/L (nM) of DNA analyte that has a complementary sequence to the lock strand, where C_0 is the initial capacitance in the absence of analyte. Increasing the negative voltage forces the structures to open, upon which we see an increase in $\Delta C_{structure}/C_0$ that saturates at ≈ –0.3 V. Upon flushing the fluidic cell with running buffer solution (RBS) to remove excess analyte (see *Materials and Methods* for buffer

composition), we observed no further change in $\Delta C_{structure}/C_0$ indicating that the analyte binding the lock strands prevented the structures from reverting to a closed state. On average, we observed that $\Delta C_{structure}/C_0$ changed by 0.08±0.01, 0.17±0.02, 0.8±0.2 and 0.7±0.3 for an applied V_{DC}–$V_{Ag/AgCl}$ of 0 V, –0.1 V, –0.2 V and –0.3 V respectively for the *normally closed* case. The observed values of $\Delta C_{structure}/C_0$ represent an ≈11-fold increase compared with the hybridization of ssDNA probe strands with a complementary sequence (ΔC_{ssDNA}=0.07±0.01). Expanded uncertainties are reported with coverage factor k=2. A smaller enhancement in $\Delta C_{structure}$ was observed for the *normally open* case as seen in Fig. 4B. Here $\Delta C_{structure}/C_0$ was found to be 0.01±0.01, 0.05±0.02, 0.2±0.08 and 0.2±0.02 for an applied V_{DC}–$V_{Ag/AgCl}$ of 0 V, +0.1 V, +0.2 V and +0.3 V respectively. While this represented an ≈3-fold higher improvement over the ssDNA hybridization case, it was comparatively lower than the *normally closed* results.

The difference in the enhancement between the two structures can be attributed to the effectiveness of the electric field (E) at actuating the hinge structure as seen from Fig. 4D. When the hinge is closed ($\theta \rightarrow 0$ rad or 0°), E is orthogonal to the top arm resulting in a large electric force (F_E) that works in concert with the hinge restoring force (F_H) to efficiently open the structure. When the hinge is open ($\theta \rightarrow \pi/2$ rad or 90°), E is parallel to the top arm and therefore applies a negligible F_E. At the open position, the hinge spring is also at its energy minimum resulting in a negligible F_H. Therefore, F_E is more effective at opening this structure than closing it. Importantly, this subtle difference translates into a drastically different signal gain.

Signal Amplification upon Binding Analyte. The signal gain (G) describes the amount of signal provided by a DNA nanostructure on analyte binding, as relative to ssDNA hybridization. This gain comes from the larger relative mass and charge of the origami, which increases capacitance, as well as from the DC bias acting on that charge, which can push the nanostructure to its final conformation. This gain is shown in Fig. 4C, and was estimated by scaling $\Delta C_{structure}$ and ΔC_{ssDNA} with the ratio of the densities of DNA probe molecules (ρ_{ssDNA}) attached to the electrode surface to the densities of the DNA origami ($\rho_{structure}$) and is given by,

$$G = \frac{\Delta C_{structure}}{\Delta C_{ssDNA}} \frac{\rho_{ssDNA}}{\rho_{structure}} \qquad (3)$$

The values of $\rho_{structure}$ and ρ_{ssDNA} were measured chronocoulometrically[34] (SI section S9) to be (6.21±0.004)×10^8 cm^{-2} and (1.19±0.001)×10^{12} cm^{-2} respectively. These estimates of surface density translate to a surface coverage of only ≈1 % for the highly charged DNA origami compared to ≈25 % for the ssDNA probes. From Fig. 4C, G increases monotonically with negative voltages for the *normally closed* structures and with positive voltages for the *normally open* structures. This trend mirrors the change in the measured capacitance in Fig. 4A and 4B. The estimated gain, relative to ssDNA hybridization, peaks at (2.1±0.1)×10^4 for the *normally closed* structures and (0.6±0.05)×10^4 for the *normally open* case before reaching a plateau. This

maximum indicates that the structures are strongly responsive to E, requiring low voltages to change their conformations. This significant signal amplification can be further improved by structural modifications to increase mobile charge displacement, by more effectively utilizing the hinge restoring force, F_H, and improving the surface attachment to the electrodes, i.e., by removing the anchor stilts.

To further quantify the amplification measured in Fig. 4C, we measured a standard curve by varying the analyte concentration for the *normally closed* structures. This is shown in Fig. 4E with measurements down to a solution analyte concentration of 1 fmol/L (fM) at V_{DC}–$V_{Ag/AgCl}$=–0.3 V and an incubation time of 15 minutes. As expected, the measured change in the capacitance relative to the case where no analyte was present decreases with lower concentration. The change in the signal at the lowest measured concentration of 1 fmol/L (fM) was considerably larger than the case with a non-complementary control sequence.

The uncertainty in the measurement (at the 95 % confidence interval) allowed us to determine the signal to noise ratio (SNR) of our measurements as seen from Fig. S10.1. This uncertainty sets the floor for the smallest measurable concentration which is significantly lower than 1 fmol/L (fM) and was determined using well-established techniques found in the literature.[14] The limit of detection (LOD) of our approach is lower than that measured using DNA binding experiments in previous work[35,36] and agrees well with our amplification factor of ≈20,000.

It is difficult to provide comprehensive performance comparisons for new and disparate receptors and modes of sensing. The metrics of interest conflate the performance of the receptor and physicochemical transducer of which a biosensor is comprised.[37] As a result when receptors are optimized and matched with different transducers, the performance can change dramatically. This is especially the case here, where DNA nanostructure signal amplifiers blur the line between receptor and transducer and can be paired with different readout schemes. Few examples exist in the literature for the signal amplification approach reported here making a direct comparison challenging. Of the most closely related examples, our estimated LOD of <1 fmol/L (fM) *via* impedance spectroscopy is better than those reported using amperometry [<1 pmol/L (pM)],[38] and impedance spectroscopy [10 pmol/L (pM) and 1 nmol/L (nM)].[14] More generally, the reported LOD for electrochemical measurements of DNA hybridization in the absence of nanostructure signal amplifiers can vary drastically depending on the transducer and electrode structure, used.[39] For example, the reported LOD of 1.5 amol/L (aM) using an interdigitated electrode is surprisingly similar to best-in-class PCR assays.[40] However, this result appears to be an outlier with most measurements reporting significantly higher LODs.[41]

In practice, achieving measurements significantly below the concentrations measured here is often confounded by the affinity of the interaction (i.e., receptors with higher binding affinities will allow improved limits of detection) and the fact that the interaction of the analyte with the

structures is limited by diffusion requiring significantly longer measurement times for the lowest concentrations and larger uncertainties due to drift.[42] Therefore, this metric is dependent both on the type of receptor analyte pair and the engineering of the system. The 20,000-fold higher sensitivity relative to DNA binding assays achieved that we demonstrate in this work using a novel, dynamic sensor helped improve the overall limit of detection.

It is also important to note that the measurements shown in the figures above were performed by repeatedly regenerating the chip using an antidote DNA sequence that utilizes strand displacement to remove any bound analyte and reset the measurement. This is apparent in Fig. S10.2 in the SI that shows a representative example where the antidote strand returns the capacitance to its baseline value (within statistical variation) after each analyte concentration is measured. The ability to perform a simple reset of the sensor with an antidote strand in this way alleviates a critical challenge with most biosensors which exhibit significant chip to chip variation that confounds analysis and intercomparison.

As we demonstrate here, DNA origami-based signal amplifiers can greatly improve electrochemical biosensing. However, there are numerous opportunities to optimize the structures to fit a wide range of applications. We can further increase the measured signal by optimizing the motion of charge in the vicinity of the surface. The locks can be redesigned to include non-nucleic acid targets. Improved impedance modeling as a function of origami angle could help identify DC biases that accelerate closing or opening. Finally, the buffer conditions could be optimized to balance ion content between maintaining structural integrity and rigidity while reducing charge screening from the electrode. Similarly, redox mediators which increase ionic conductivity could be tuned to minimize noise in the measured capacitance.

Another exciting direction for integrating new capabilities in these structures lies in modifying the number and function of the lock positions. Multiple lock positions would increase or decrease the hinge sensitivity for the normally open and normally closed systems respectively as they would function in parallel. More interestingly, the combination of normally open and closed motifs in the same structure, combined with strand displacement logic from the DNA computation community,[43] can enable complex response based on the input of multiple analytes.

Conclusions

As DNA origami are readily designed into custom geometries that support engineered dynamic properties, they will provide robust and specific signal conditioning in electric measurements of biomolecular binding. As we show here, we can engineer DNA origami that move significant charge near electrode surfaces or allow conformation control *via* an applied DC bias to tune signal amplification.

To the best of our knowledge, we are unaware of DNA origami used for biosensing where electric fields were used to both control and transduce the sensor signal. This feature sets apart our results from those found in the literature. As we show here, these interfaces comprised of simple hinge-based geometries allow dramatically improved gain as high as $\approx 2\times10^4$ compared to ssDNA hybridization under comparable conditions and be used reversibly for multiple measurements. While the increased charge and mass associated with signal amplification can slow the timescales associated with structural motion, our demonstration of using the DC field to control conformation diminishes this concern. In short, these engineered nanostructures amplify the signal from specific, desired, binding interactions while reducing the contribution from non-specific surface binding.

In future work we plan to explore the many avenues available to improve signal conditioning through re-engineering of the DNA origami. These include shortening the thiol anchors to bring the structure closer to the surface, tuning the interaction of the structure with the surface, or varying the hinge geometry, lock position and arrangement. The wide and varied opportunities for optimization both through the DNA origami design and the measurement conditions, i.e. buffer or voltage conditions, and through the origami design indicates that the gain observed here could be improved. Finally, we anticipate implementation of DNA computation techniques which could integrate molecular logic gates into these systems.

Beyond the pathways to improved signal amplification our approach has the potential to modify the energetics and kinetics of binding for arbitrary analytes leading to highly tunable sensing interfaces. This will open broad research directions to develop frameworks to incorporate different lock types such as aptamers, and for modifying the dynamic motion of the structures.

Materials and Methods

DNA Nanostructure synthesis

The sequences used for the DNA origami were derived from previous work,[27] except for the modifications discussed in SI section S1. The P8064 M13 sequence was used as a scaffold at a concentration of 35 nmol/L. The staples, suspended in 40 mmol/L Tris, 20 mmol/L acetic acid, 1 mmol/L EDTA (TAE) buffer and 12.5 mmol/L $MgCl_2$ in deionized water (DIW), were introduced at a 10-fold higher concentration than the scaffold (350 nmol/L). The DNA staples were annealed with the scaffold for 12 hours from 80 ˚C to 4 ˚C. A centrifugal spin filter with a 100 kDa molecular weight cutoff was used to remove excess staples through five iterative additions of 0.5 mL of buffer. The samples were stored at 4 ˚C. DNA samples for Cryo-EM microscopy were annealed with 80 nmol/L scaffold.

Gold Electrode Functionalization

Commercially sourced gold electrodes were prepared for electrochemical measurements by cleaning and functionalization via co-incubation with mercaptohexanol (MCH) and thiol labeled DNA origami. The electrodes were first cleaned by immersing them in nanostrip for 10 minutes followed by thoroughly rinsing them in DIW. The electrodes were then further cleaned electrochemically in a solution of 50 mmol/L of sulfuric acid (H_2SO_4) by sweeping a voltage from −0.5 V to +1 V relative to an Ag/AgCl pseudo reference electrode at a rate of 0.1 V/s. The sweeps were repeated for a minimum of 10 cycles and until the reduction peak reached a steady state. The substrates were then washed with DIW. Running buffer solution (RBS) comprised of TAE with 50 mmol/L NaCl, 12.5 mmol/L $MgCl_2$, 200 μmol/L K_3 $Fe(CN)_6$ and 200 μmol/L K_4 $Fe(CN)_6$ was prepared and used both for modifying the surfaces and for the electrochemical measurements. The cleaned chips were incubated for >18 hours at room temperature in RBS with 10 nmol/L of the thiol labeled DNA origami, 10 nmol/L of mercaptohexanol (MCH) for surface passivation of the unreacted gold and 10 μmol/L Tris (2-carboxyethyl) phosphine (TCEP) as reducing agent. The chips were then thoroughly washed with RBS before being used for electrochemical measurements. The surface attachment chemistry was validated by using capacitance measurements as described in SI section 11. Chronocoulometric measurements were performed by adding 50 μmol/L of Hexaammineruthenium(III) chloride (RuHex) to RBS.

Electrochemical Measurements

All electrochemical impedance spectroscopy measurements were performed with a two-electrode electrochemical cell with a 200 μL sample volume. An impedance analyzer was used to apply an AC voltage with an amplitude of V_{pk}=20 mV over a frequency range of 0.5 Hz to 200 kHz and measure the resulting current. Baseline measurements were performed with RBS and again after incubating with analyte for an incubation time specified in the main text followed by rinsing the cell with RBS to remove excess analyte. All capacitance measurements were performed at a fixed frequency of 100 Hz, AC voltage amplitude of V_{pk}=20 mV and by sweeping the DC voltage from −0.4 V to +0.4 V relative to an Ag/AgCl pseudo reference electrode.

Cryogenic Electron Microscopy:

CryoEM measurements were performed to reconstruct the DNA origami. Reconstructing entire hinge was difficult due to their flexibility and would likely require larger particle numbers and flexible refinement methods that were beyond the scope of this work. However, we visualized the 3D arrangement of helices within the hinge arms by picking and analyzing each arm (half-hinge) as independent particle using standard single-particle analysis methods. A detailed description of the measurements and reconstruction techniques are provided in SI section S8.

References

1 P. W. K. Rothemund, *Nature*, 2006, **440**, 297–302.
2 A. E. Marras, L. Zhou, H.-J. Su and C. E. Castro, *Proc. Natl. Acad. Sci.*, 2015, **112**, 713–718.
3 S. Dey, C. Fan, K. V. Gothelf, J. Li, C. Lin, L. Liu, N. Liu, M. A. D. Nijenhuis, B. Saccà, F. C. Simmel, H. Yan and P. Zhan, *Nat. Rev. Methods Primer*, 2021, **1**, 1–24.
4 S. Wang, Z. Zhou, N. Ma, S. Yang, K. Li, C. Teng, Y. Ke and Y. Tian, *Sensors*, 2020, **20**, 6899.
5 A. R. Chandrasekaran, J. A. Punnoose, L. Zhou, P. Dey, B. K. Dey and K. Halvorsen, *Nucleic Acids Res.*, 2019, **47**, 10489–10505.
6 T. Funck, F. Nicoli, A. Kuzyk and T. Liedl, *Angew. Chem. Int. Ed.*, 2018, **57**, 13495–13498.
7 V. V. Thacker, L. O. Herrmann, D. O. Sigle, T. Zhang, T. Liedl, J. J. Baumberg and U. F. Keyser, *Nat. Commun.*, 2014, **5**, 3448.
8 K. Trofymchuk, K. Kołątaj, V. Glembockyte, F. Zhu, G. P. Acuna, T. Liedl and P. Tinnefeld, *ACS Nano*, 2023, **17**, 1327–1334.
9 D. Minev, C. M. Wintersinger, A. Ershova and W. M. Shih, *Nat. Commun.*, 2021, **12**, 1741.
10 J. M. Majikes, L. C. C. Ferraz and T. H. LaBean, *Bioconjug. Chem.*, 2017, **28**, 1821–1825.
11 S. Julin, V. Linko and M. A. Kostiainen, *ACS Nano*, 2023, **17**, 11014–11022.
12 F. Kroener, A. Heerwig, W. Kaiser, M. Mertig and U. Rant, *J. Am. Chem. Soc.*, 2017, **139**, 16510–16513.
13 Y. Chang, X. Tang, J. Huang, Y. Chai, Y. Zhuo, H. Li and R. Yuan, *Anal. Chem.*, 2021, **93**, 12075–12080.
14 P. Williamson, P. Piskunen, H. Ijäs, A. Butterworth, V. Linko and D. K. Corrigan, *ACS Sens.*, 2023, **8**, 1471–1480.
15 M. Tayyab, D. Barrett, G. van Riel, S. Liu, B. Reinius, C. Scharfe, P. Griffin, L. M. Steinmetz, M. Javanmard and V. Pelechano, *Sci. Adv.*, 2023, **9**, eadi4997.
16 S. Liu, J. Wu, S. Li and L. Wang, *Anal. Chem.*, 2023, **96**, 828–838.
17 V. Walawalkar, M. S. Sajal, Y. Gilpin, M. Dandin and R. E. Taylor, 2023, 2023.03.02.530881.
18 S. M. Robinson, Z. Shen, J. R. Askim, C. B. Montgomery, H. O. Sintim and S. Semancik, *Biosensors*, 2019, **9**, 54.
19 Y. Xiao, R. Y. Lai and K. W. Plaxco, *Nat. Protoc.*, 2007, **2**, 2875–2880.
20 M. Lin, P. Song, G. Zhou, X. Zuo, A. Aldalbahi, X. Lou, J. Shi and C. Fan, *Nat. Protoc.*, 2016, **11**, 1244–1263.
21 R. Qing, M. Xue, J. Zhao, L. Wu, A. Breitwieser, E. Smorodina, T. Schubert, G. Azzellino, D. Jin, J. Kong, T. Palacios, U. B. Sleytr and S. Zhang, *Sci. Adv.*, 2023, **9**, eadf1402.
22 G. Ortega, A. Chamorro-Garcia, F. Ricci and K. W. Plaxco, *Annu. Rev. Biophys.*, 2023, **52**, 319–337.
23 C. Ye, M. Wang, J. Min, R. Y. Tay, H. Lukas, J. R. Sempionatto, J. Li, C. Xu and W. Gao, *Nat. Nanotechnol.*, 2024, **19**, 330–337.
24 J. M. Majikes and J. A. Liddle, *Nanoscale*, 2022, **14**, 15586–15595.
25 G. Liu, *Front. Bioeng. Biotechnol.*
26 Y. Wang, X. Jin and C. Castro, 2023, 2023.05.11.540408.
27 M. Darcy, K. Crocker, Y. Wang, J. V. Le, G. Mohammadiroozbahani, M. A. S. Abdelhamid, T. D. Craggs, C. E. Castro, R. Bundschuh and M. G. Poirier, *ACS Nano*, 2022, **16**, 5682–5695.

28 Y. Wang, J. V. Le, K. Crocker, M. A. Darcy, P. D. Halley, D. Zhao, N. Andrioff, C. Croy, M. G. Poirier, R. Bundschuh and C. E. Castro, *Nucleic Acids Res.*, 2021, **49**, 8987–8999.
29 X. Liu, J. Song, R. Yang, S. Su, L. Zhang, Y. Huang and Q. Fan, *IEEE Sens. J.*, 2022, **22**, 12460–12472.
30 Bard, Allen J. and Faulkner, Larry R., *Electrochemical Methods: Fundamentals and Applications*, Wiley, 2nd edn., 2000.
31 E. A. Josephs and T. Ye, *J. Am. Chem. Soc.*, 2012, **134**, 10021–10030.
32 S. O. Kelley, J. K. Barton, N. M. Jackson, L. D. McPherson, A. B. Potter, E. M. Spain, M. J. Allen and M. G. Hill, *Langmuir*, 1998, **14**, 6781–6784.
33 S. Modi, D. Bhatia, F. C. Simmel and Y. Krishnan, *J. Phys. Chem. Lett.*, 2010, **1**, 1994–2005.
34 A. B. Steel, T. M. Herne and M. J. Tarlov, *Anal. Chem.*, 1998, **70**, 4670–4677.
35 S. Cho, A. Zaslavsky, C. A. Richter, J. M. Majikes, J. A. Liddle, F. Andrieu, S. Barraud and A. Balijepalli, in *2022 International Electron Devices Meeting (IEDM)*, 2022, p. 24.2.1-24.2.4.
36 S. T. Le, N. B. Guros, R. C. Bruce, A. Cardone, N. D. Amin, S. Zhang, J. B. Klauda, H. C. Pant, C. A. Richter and A. Balijepalli, *Nanoscale*, 2019, **11**, 15622–15632.
37 D. R. Thévenot, K. Toth, R. A. Durst and G. S. Wilson, *Biosens. Bioelectron.*, 2001, **16**, 121–131.
38 B. Jeon, M. M. Guareschi, J. M. Stewart, E. Wu, A. Gopinath, N. Arroyo-Currás, P. Dauphin-Ducharme, P. S. Lukeman, K. W. Plaxco and P. W. K. Rothemund, 2023.
39 J.-Y. Park and S.-M. Park, *Sensors*, 2009, **9**, 9513–9532.
40 R. Arnaout, R. A. Lee, G. R. Lee, C. Callahan, C. F. Yen, K. P. Smith, R. Arora and J. E. Kirby, 2020, 2020.06.02.131144.
41 J. Baranwal, B. Barse, G. Gatto, G. Broncova and A. Kumar, *Chemosensors*, 2022, **10**, 363.
42 X. Duan, Y. Li, N. K. Rajan, D. A. Routenberg, Y. Modis and M. A. Reed, *Nat. Nanotechnol.*, 2012, **7**, 401–407.
43 J. Yin, J. Wang, R. Niu, S. Ren, D. Wang and J. Chao, *Chem. Res. Chin. Univ.*, 2020, **36**, 219–226.